Springer

Acta Mechanica Sinica

CrossMark click for updates

• RESEARCH PAPER •

Acta Mech. Sin., Vol. 39, 122387 (2023)
https://doi.org/10.1007/s10409-022-22387-x

Statistics of temperature and velocity fluctuations in supergravitational convective turbulence

Dongpu Wang[1], Jing Liu[1], Quan Zhou[2*], and Chao Sun[1,3*]

[1] *Center for Combustion Energy, Key Laboratory for Thermal Science and Power Engineering of MoE, and Department of Energy and Power Engineering, Tsinghua University, Beijing 100084, China;*
[2] *Shanghai Key Laboratory of Mechanics in Energy Engineering, Shanghai Institute of Applied Mathematics and Mechanics, School of Mechanics and Engineering Science, Shanghai University, Shanghai 200072, China;*
[3] *Department of Engineering Mechanics, School of Aerospace Engineering, Tsinghua University, Beijing 100084, China*

Received October 28, 2022; accepted November 8, 2022; published online December 8, 2022

We report an experimental study of the temperature and velocity fluctuations in supergravitational turbulent convection system. The negative spikes of the time series of temperature fluctuations appear periodically, which may result from the azimuthal movement of the cold plumes in the rotating frame pushed by the zonal flow. The period τ_0 decreases slightly with increasing Rayleigh number (Ra) and τ_0 is over one order larger than the time scale of the large-scale circulation. In addition, the temperature frequency power spectra follow $P(f) \sim f^{-5}$ for different Ra over the range $2 \lesssim f \lesssim 10$, implying the possible existence of inverse cascade due to turbulence in equilibrium with zonal flow. The Rhines frequency f_β at which the inverse cascade ceases is around half of a decade smaller than the smallest frequency of the –5 scaling range. Further, the azimuthal distribution of the time-averaged radial velocity has no obvious peak and trough, which provides further evidence for the existence of zonal flow. Additionally, it is found that the probability density function for temperature and velocity fluctuations in the current system can be well fitted with the model (Wang et al. 2019, 2022) for the classical Rayleigh-Bénard convection.

Turbulent convection, Supergravity, Probability density function, Power spectra, Zonal flow

Citation: D. Wang, J. Liu, Q. Zhou, and C. Sun, Statistics of temperature and velocity fluctuations in supergravitational convective turbulence, Acta Mech. Sin. **39**, 122387 (2023), https://doi.org/10.1007/s10409-022-22387-x

1. Introduction

Turbulent convection is a common phenomenon in nature and engineering settings. Rayleigh-Bénard convection (RBC) is a paradigm model for studying thermal turbulence [1]. Experiments of RBC are mostly conducted in a cell heated from below and cooled from above. Rectangular or cylindrical sidewalls are required to confine the flow [2, 3]. Recently, Jiang et al. [4], Rouhi et al. [5], and Wang et al. [6, 7] have put forward annular centrifugal Rayleigh-Bénard convection (ACRBC), in which the fluid layer is heated from the outer cylinder and cooled from the inner cylinder under a solid body rotation around the axis of the cylinders (generating supergravity). Exploiting Einstein's equivalence principle, from the Earth's frame to a strongly rotating reference frame, the Rayleigh number (an important control parameter in the problem of RBC) can be increased largely in ACRBC due to the supergravity.

An important issue in the study of thermal turbulence is the statistical properties of the turbulent fluctuations [8]. In the past decades, there has been a large number of studies of small-scale temperature and velocity fluctuations in convective turbulence (see Refs. [8, 9], for reviews of the properties of turbulent fluctuations in buoyancy-driven turbulent flow). Many experimental studies focused on the statistics of the temperature [10-15], while corresponding studies in the velocity measurement are relatively difficult and scarce

*Corresponding authors. E-mail addresses: qzhou@shu.edu.cn (Quan Zhou); chaosun@tsinghua.edu.cn (Chao Sun)
Executive Editor: Keqing Xia

[14, 16]. Additionally, ACRBC is a novel system to study turbulent convection [4]. The statistical properties of the turbulent fluctuations in ACRBC are still elusive.

Statistical properties of turbulent fluctuations are often studied from the probability density distribution and the energy cascade [17]. A characteristic flow structure of turbulent RBC is the thermal plumes [18], detaching from the thermal boundary layers (BLs) intermittently, which causes the probability density function (PDF) of fluctuations to exhibit an exponential tail [10-12, 19-22]. Wang et al. [10, 11] divided the flow region into the turbulent bulk, mixing zone, sidewall region, and BLs. It is found that the PDFs of the temperature fluctuation δT are different in these regions. What do the PDFs of temperature and velocity fluctuations in different regions compare in ACRBC? Recent work [4-6] suggests that the heat transport and many of the flow features like plumes and large-scale circulation rolls (LSCR) in ACRBC are similar to those of traditional RBC. Does this also mean that the effects of plumes and LSCR on the PDFs are also similar for ACRBC and RBC? Answering these questions will be one of the objectives of the present study.

In addition, strong rotation could modify the nature of turbulence [23]. For example, zonal flows have been shown to emerge due to the topographic β-effect [24-26]. Rhines [26] deduced that zonal flow is typically on a scale k_β which is called as Rhines scale:

$$k_\beta = \sqrt{\beta/(2U)}\,, \tag{1}$$

where k_β is the characteristic wavenumber, β is the mean value of the gradient of the Coriolis frequency, and U is the typical velocity. Rhines considers the inverse cascade from small to large scales ceases at the Rhines scale and the energy spectrum is

$$E(k) \sim k^{-5}\,. \tag{2}$$

The flow in ACRBC is similar to the flow in the equatorial region of the planets. A similar zonal flow is also observed in the current ACRBC system [4-6], and this zonal flow is the convection rolls revolving around the rotating axis in the rotating frame that is caused by the asymmetric movement of warm and cold plumes. What are the properties of energy cascade combining the effects of buoyancy with strong rotation? This is one question that this study aims to address.

In this paper, we report results from local temperature and velocity measurements in an ACRBC cell filled with water. The remainder of this paper is organized as follows. In Sect. 2, we give a brief description of the experimental methods. The results are presented and discussed in Sect. 3, which is divided into two parts, including the analyses of the temperature (Sect. 3.1) and velocity fluctuations (Sect. 3.2). Finally, the work is summarized in Sect. 4.

2. Methodology

2.1 Parameter descriptions

In ACRBC, the flow is driven by the centrifugal buoyancy and affected by the Coriolis force. The dynamics of the flow are determined by the geometry of the cell and three dimensionless parameters:

$$Ra = \frac{1}{2}\omega^2(R_o + R_i)\alpha\Delta L^3/(\nu\kappa)\,, \tag{3}$$

which reflects the buoyancy-driven strength,

$$Pr = \nu/\kappa\,, \tag{4}$$

which reflects the ratio of momentum diffusivity to thermal diffusivity,

$$Ek = \nu/(2\omega L^2)\,, \tag{5}$$

which indicates the ratio of viscous force to Coriolis force. Note that Coriolis effects can be alternatively reflected by the Rossby number. Here, ω denotes the angular velocity of the system, $L = R_o - R_i$ is the gap width in which R_o and R_i are the radius of the outer and inner cylinders, $\Delta = T_{\rm hot} - T_{\rm cold}$ is the temperature difference in which $T_{\rm hot}$ and $T_{\rm cold}$ are the temperature of the outer and inner cylinders. α, ν, and κ are the thermal expansion coefficient, kinematic viscosity, and thermal diffusivity, respectively. As shown in Table I, the experiments are conducted for Ra in the range of $[4.05 \times 10^9, 2.85 \times 10^{10}]$, fixed $Pr \simeq 4.2$ corresponding to the water at around 40 °C, fixed $Ek \simeq 6.7 \times 10^{-7}$, and radius ratio $\eta = R_i/R_o = 0.5$. An additional dimensionless control parameter, the Ekman number, appears for supergravitational convective turbulence. The measurements are made at fixed $Ek \simeq 6.7{\times}10^{-7} \ll 1$, suggesting the Coriolis effects are much stronger than the viscous force. We note that $Ek \sim O(10^{-7})$ is a relatively small value in the study of rotating turbulent flows (see Ref. [27], for a review of rapidly-rotating convection), while it is still much larger than that in planetary cores. For example, $Ek \approx 10^{-15}$ in the Earth's core [28] in which viscosity is very low.

2.2 Laboratory experiments

The experimental setup was detailed elsewhere [4]. The apparatus is a cylindrical annulus with nickel plated copper outer and inner walls of $R_o = 240$ mm and $R_i = 120$ mm (see Fig. 1a and b). The gap with a height $H = 120$ mm is sandwiched by a top and bottom polycarbonate plate. Thus, the radius ratio is $\eta = 0.5$ and aspect ratio $\Gamma = H/L = 1$. Polycarbonate with excellent properties such as transparency, high heat deformation temperature ($\simeq 130$ °C), and low thermal conductivity ($\simeq 0.2$ W/(m K)) is suitable for the material

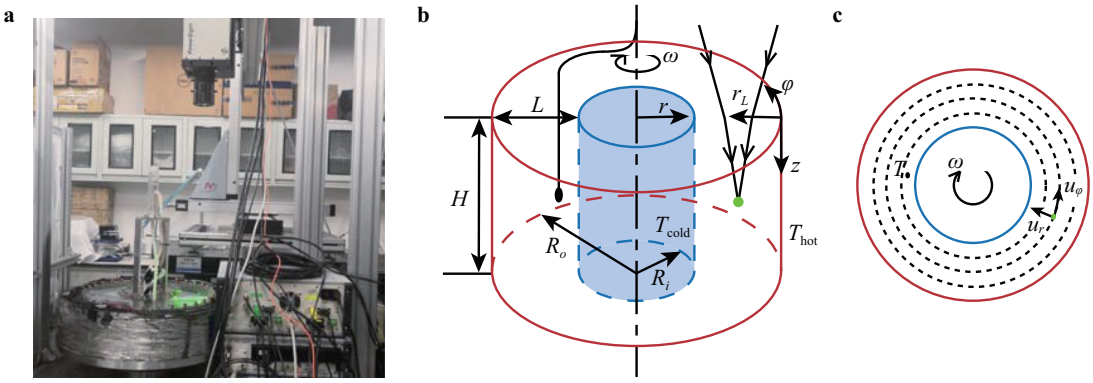

Figure 1 Experimental configuration. **a** A photograph of the annular centrifugal convection cell (left), laser probe of LDV (top), and devices for photoelectric signal acquisition and processing (right). **b** Sketch of the experimental set-up, which defines the coordinate frame for the LDV measurements and geometric parameters. **c** Top view of the sketch of the convection cell. The dotted points denote the three sets of measured points at $R' \simeq 0.25$ (inner mixing zone, $R' \in [\delta_{\rm th}, 0.3]$), $R' \simeq 0.5$ (cell centre) and $R' \simeq 0.75$ (outer mixing zone, $R' \in [0.7, 1-\delta_{\rm th}]$). The system rotates clockwise for all cases.

of the sidewalls, allowing the laser light to measure the flow and reducing the lateral heat flux out of and into the cell. The temperature of the inner cylinder is regulated by passing coolant liquid. The outer cylinder is heated at a constant rate with an embedded film heater and direct current (DC) power supply. The temperatures of the inner and outer cylinders are monitored by thermistors (Omega, 44031) embedded inside the cylindrical walls. We confirm the flow reaches the statistically stationary state, which is determined by the convergence of the global Nu number (listed in Table I). The experimental conditions are also listed in Table I (documented in Appendix A).

To measure the temperature fluctuations, another type of thermistor (Amphenol, FP07DA103N) with small diameter ($\simeq$ 1 mm) and ultra-fast response time of 7 ms is inserted into the flow at $R' \equiv (r - R_i)/L \simeq 0.2$ (Fig. 1b). Note that the thermistor is rotated with the system so the azimuthal position of the measurement is fixed. The sampling rate of the local temperature fluctuations is 128 Hz. In addition, we adopt laser Doppler velocimetry (LDV: TSI Inc., USA, type LDV01010) to measure the velocity fluctuations. Some hollow glass beads as tracers with density $\rho_p \simeq 1.05$ g/cm^3 and diameter $d_p \simeq 5$ μm are mixed into the degassed water. The beams of the LDV are in the rz-plane and ϕz-plane (not shown), corresponding to the measurements of the radial velocity u_r and azimuthal velocity u_ϕ, respectively. Note that in our previous study of supergravitational convection [4, 6, 7], the definition of the direction of the radial position is the same as r in Fig. 1b of the manuscript. While the definition of the direction of the wall-normal coordinate in classical RBC (usually use z) is from the hot plate to the cold plate [10, 11], which is the same as r_L (the definition used for the LDV measurements) in Fig. 1b of the manuscript. In a typical run, the mean sampling rate of u_r is around 1500 Hz, while the mean data rate for u_ϕ is relatively low ($\lesssim$ 200 Hz) because of the large rotation speed of the rotating system. The measurements last for 1 h typically. We can vary the coordinate (r,ϕ,z) of the LDV probe through the traverse system (Isel, LES5-3-L890). In order to reduce the effects of the top and bottom plates, the measurements are at mid-axial position $z = 0.5H$ (Fig. 1b). Figure 1c shows the radial measurement points for probability density statistics of velocity fluctuations, which are at $R' \simeq 0.25$ (inner mixing zone), $R' \simeq 0.5$ (cell centre) and $R' \simeq 0.75$ (outer mixing zone), and the radial position $R' \simeq 0.2$ for the measurement of temperature.

3. Results and discussion

As already mentioned, to our knowledge, there are no experimental measurements of the statistical properties of the temperature and velocity fluctuations in ACRBC. High-precision measurements and careful analyses of the statistical properties of the temperature and velocity fluctuations can thus shed light on the complex supergravitational turbulent flow.

3.1 Temperature fluctuation

Figure 2a-d shows the time series of the local temperature at $R' \simeq 0.2$ after the system has reached the statistically stationary state. The corresponding PDFs of the temperature fluctuations are shown in Fig. 2e. As the heat transport properties and large-scale flow structure of ACRBC are similar to classical RBC in this Ra regime [4], the flow region is divided into BL region ($R' \in [0, \delta_{\rm th}] \cup [1-\delta_{\rm th}, 1]$), mixing zone ($R' \in [\delta_{\rm th}, 0.3] \cup [0.7, 1-\delta_{\rm th}]$), turbulent bulk ($R' \in [0.3, 0.7]$) [11]. In this Ra range, the thickness of thermal BL $\delta_{\rm th} \simeq L/(2Nu) \simeq 0.6$ mm. So the thermistor is located at the inner mixing zone. Figure 2e shows that at

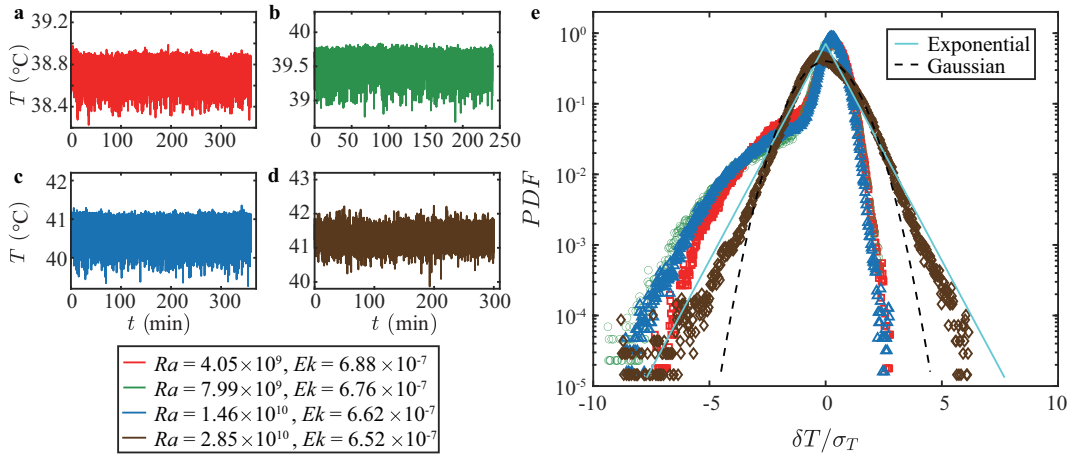

Figure 2 **a-d** Time series of the local temperature measured at $R' \simeq 0.2$ and $z = 0.5H$ for $Ek \simeq 6.7\times10^{-7}$ and different Ra. The measurements last at least 4 h after the system has reached the statistically stationary state. **e** Corresponding PDF of the measured temperature fluctuations $\delta T/\sigma_T$, where $\delta T(t) = T(t) - \langle T\rangle_t$ and σ_T is r.m.s. value of δT. The black dashed line in **e** shows the Gaussian function given in Eq. (7). The celeste solid line in **e** is the exponential function given in Eq. (6).

$Ra \lesssim 1.46\times10^{10}$, the PDF of $\delta T/\sigma_T$ are similar, which have large negative wings. The cold plumes detached from the inner cylinder may contribute to the large negative fluctuations. We note that the PDF of the negative $\delta T/\sigma_T$ falls off less steeply than the exponential function as suggested by He et al. [12]:

$$P(\delta/\sigma) = \frac{1}{\sqrt{2}\sigma} \mathrm{e}^{-\sqrt{2}|\delta/\sigma|}, \tag{6}$$

which implies the strength and number of cold plumes are more than that at the cell center of the traditional RBC. As Ra increases to $Ra = 2.85\times10^{10}$, i.e., the highest Ra of the present study, the PDF is obviously different from the other three cases. The core distribution at $Ra = 2.85\times10^{10}$ is more like Gaussian distribution:

$$G(\delta/\sigma) = \frac{1}{\sqrt{2\pi}\sigma} \mathrm{e}^{-(\delta/\sigma)^2/2}, \tag{7}$$

and the wings of the PDF basically conform to the exponential distribution Eq. (6). The reason for the different shapes of the PDF may be due to the scale of plumes being smaller with increasing Ra. As discussed detailedly below, we consider that the negative spikes are probably the signal of zonal flow, which pushes the cold plumes moving in a prograde/retrograde direction and the cold plume arms trigger the periodic-like temperature signals.

Recently, Wang et al. [10,11] provided a theoretical framework with a set of parameters to quantitatively describe the effect of the turbulent background, single/collective thermal plumes, and their spatio-temporal intermittency on the PDF of temperature fluctuations. In the present study of ACRBC, it is found that the PDF can be classified into two types (see Fig. 3). At $Ra = 2.85\times10^{10}$, the fluctuations of cold and warm plumes are similar. The PDF profile is more approximate to the form of Eq. (4.13) in Wang et al. [10], which is rewritten in Eq. (8):

$$\begin{aligned} P(\delta/\sigma;\alpha_w,\alpha_c,\beta) = {} & \frac{(1-\beta)\gamma_2}{2} \exp\left[\alpha_c^2/2 + \gamma_2(\delta/\sigma) + \beta\alpha_c/\alpha_w - 1\right] \mathrm{erfc}\left[\frac{\alpha_c^2 + \gamma_2(\delta/\sigma) + \beta\alpha_c/\alpha_w - 1}{\sqrt{2}\alpha_c}\right] \\ & + \frac{\beta\alpha_w\gamma_2}{2(\alpha_w+\alpha_c)} \exp\left[\alpha_w^2/2 - \gamma_1(\delta/\sigma) + \alpha_w/\alpha_c - \beta\right] \mathrm{erfc}\left[\frac{\alpha_w^2 - \gamma_1(\delta/\sigma) + \alpha_w/\alpha_c - \beta}{\sqrt{2}\alpha_w}\right] \\ & + \frac{\beta\alpha_w\gamma_2}{2(\alpha_w+\alpha_c)} \exp\left[\alpha_c^2/2 + \gamma_2(\delta/\sigma) + \beta\alpha_c/\alpha_w - 1\right] \mathrm{erfc}\left[\frac{\alpha_c^2 + \gamma_2(\delta/\sigma) + \beta\alpha_c/\alpha_w - 1}{\sqrt{2}\alpha_c}\right], \end{aligned} \tag{8}$$

which includes the parameters $\alpha_c = \sigma_B/\sigma_c$, $\alpha_w = \sigma_B/\sigma_w$, and β. Here, σ_B, σ_c, and σ_w are the root-mean-square (r.m.s.) values of the fluctuations contributed by turbulent background, cold plumes, and warm plumes, respectively. β characterizes the spatio-temporal intermittency. Figure 3 shows that the experimental data are in good agreement with the theoretical model. In Fig. 3, the fit of Eq. (8) to the data measured in the mixing zone of the classical RBC is also plotted

for comparison [10]. For $Ra \in [4.05\times10^9, 1.46\times10^{10}]$, as the strength of the negative fluctuations is much stronger than the positive part, the profile is more like the PDF measured in the outer BL region of classical RBC (see Fig. 4 or 5 in Wang et al. [11]), corresponding to Eq. (2.14) in Wang et al. [11], which is rewritten in Eq. (9):

$$
\begin{aligned}
P(\delta/\sigma;\alpha_c,n_c,\beta_{sc},\beta_{mc}) = {} & \frac{(1-\beta_{sc}-\beta_{mc})\chi_1}{\sqrt{2\pi}}\exp\left\{-\frac{[\chi_1(\delta/\sigma)+\chi_2]^2}{2}\right\} \\
& + \frac{\beta_{sc}\alpha_c\chi_1}{2}\exp\left\{\frac{\alpha_c^2}{2}-\alpha_c[\chi_1(\delta/\sigma)+\chi_2]\right\} erfc\left[\frac{\alpha_c-\chi_1(\delta/\sigma)-\chi_2}{\sqrt{2}}\right] \\
& + \frac{\beta_{mc}2^{(n_c-3)/2}\alpha_c^{n_c}\chi_1}{\sqrt{\pi}\Gamma(n_c)}\exp\left\{-\frac{[\chi_1(\delta/\sigma)+\chi_2]^2}{2}\right\}\left\{\Gamma\left(\frac{n_c}{2}\right)\cdot{}_1F_1\left[\frac{n_c}{2},\frac{1}{2},\frac{(\alpha_c-\chi_1(\delta/\sigma)-\chi_2)^2}{2}\right]\right. \\
& \left. + \sqrt{2}\Gamma\left(\frac{n_c+1}{2}\right)\cdot[\chi_1(\delta/\sigma)+\chi_2-\alpha_c]\cdot{}_1F_1\left[\frac{n_c+1}{2},\frac{3}{2},\frac{(\alpha_c-\chi_1(\delta/\sigma)-\chi_2)^2}{2}\right]\right\}.
\end{aligned}
\tag{9}
$$

Two additional parameters appear in the fit function, cold plume number n_c and β_{mc} which reflects the collective effect of multiple-cold plumes. The obtained values of the fitted parameters are listed in Tables II and III (documented in Appendix B). The magnitude of $\beta \lesssim 0.1$ is smaller than that of classical RBC, which suggests that the intermittency effect is relatively weak in ACRBC. Note that the property of weak intermittency in ACRBC is also found in our previous work by studying the structure functions [7]. In addition, the fitted values of $\alpha_c = \sigma_B/\sigma_c$ in the mixing zone of ACRBC are smaller than 1 for most cases, which suggests that the contribution of cold plumes to the local temperature fluctuations is larger than the turbulent background.

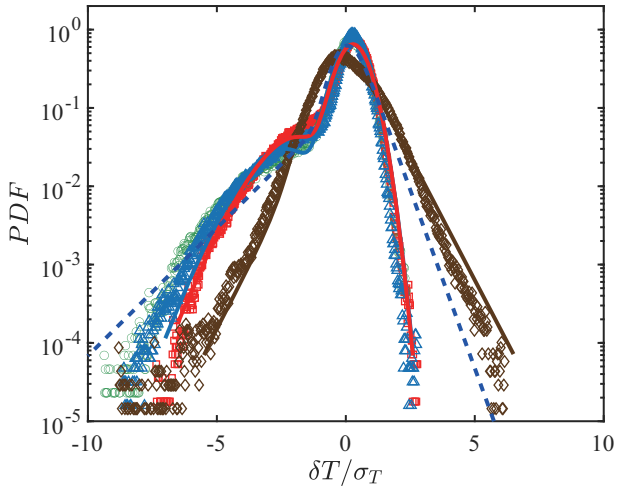

Figure 3 Fits of the theoretical models proposed by Wang et al. [10, 11] to the measured PDF data points. For $Ra = 2.85\times10^{10}$, the fit function adopts Eq. (4.13) in Wang et al. [10], i.e., Eq. (8) rewritten in this paper. For $Ra \in [4.05\times10^9, 1.46\times10^{10}]$, the fit function uses Eq. (2.14) in Wang et al. [11], i.e., Eq. (9) rewritten in this paper. The symbols share the same control parameters as Fig. 2. The solid lines are the best fits of the data points with the corresponding colors. The dashed line is the fit of Eq. (8) to the data measured in the mixing zone of the classical RBC for comparison [10]. The fitted parameters are listed in Tables II and III (documented in Appendix B).

The left inset of Fig. 4a displays the enlarge plot of the Fig. 2c at 0 s $\le t \le$ 1200 s. The amplitude of the periodic temperature spikes ($\delta T_s \gtrsim 1$ K) is significantly larger than the fluctuations of the turbulent background ($\delta T_b \simeq 0.3$ K). Further, to study the period of the spikes more quantitatively, we examine the autocorrelation function of the temperature fluctuations $C(\tau) = \langle \delta T(t+\tau)\delta T(t)\rangle / \left\langle \delta T(t)^2 \right\rangle$ (Fig. 4a). It is seen that the periodicity of the cold plumes is obvious and the near-zero peak value τ_0 is identified as the period of the spikes. $C(\tau)$ remains correlated for many periods, implying this periodic fluctuation of the flow is highly coherent. It is also found that τ_0 decreases with increasing Ra, while no obvious period is observed at $Ra = 2.85\times10^{10}$. Does this periodic fluctuation result from the large-scale circulation (LSC) observed in traditional RBC? We consider that it is not due to the LSC. The velocity of the LSC can be estimated by [29,30]

$$U_{\mathrm{LSC}} \approx 0.2(\nu/L)\sqrt{Ra/Pr}\,, \tag{10}$$

and the time scales of the LSC $\tau_{\mathrm{LSC}} = L/U_{\mathrm{LSC}}$ are calculated and denoted as the black circles in the right inset of Fig. 4a. It is found that $\tau_{\mathrm{LSC}} \ll \tau_0$ for each Ra. Here, given that the LSC structure driven by buoyancy force appears both in classical RBC and ACRBC, we assume that the characteristic velocities of classical RBC and ACRBC at the same Ra are similar. In the part of Sect. 3.2 of the manuscript, we calculate the mean of the typical large positive and negative values of the time series of u_r at $Ra = 4.05\times10^9$, which corresponds to the velocity of the coherent plumes. We can estimate the time scale of the LSC $\tau_{\mathrm{LSC}} = L/U_{\mathrm{LSC}} = 0.12/0.13 \simeq 0.92$ s, which is of the same order of magnitude as the estimation by the empirical Eq. (10). The results are similar for other Ra cases.

We consider that large negative excursions may result from the zonal flow. Zonal flow or Rossby wave is a common flow

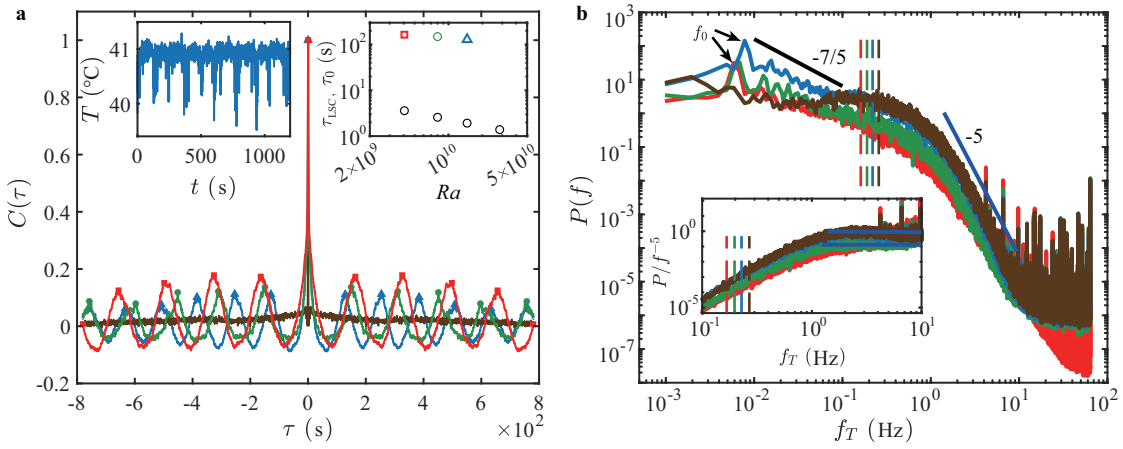

Figure 4 **a** Autocorrelation functions $C(\tau)$ of $\delta T(t)$. The left inset of **a** is the enlarge plot of Fig. 2c. Right inset of **a**: the black circles denote the time scales of the large-scale circulation τ_{LSC}. Other symbols denote the near-zero peak value τ_0 of **a** with the same color. **b** PS of $\delta T(t)$. The value "–5" denotes the slope of the reference line. The vertical lines denote the Rhines frequencies f_β for each Ra. The inset of **b** is the compensated plot. The colors of the lines share the same conditions as Fig. 2.

phenomenon observed in astrophysical flows [24,31,32]. The reason for zonal flow in ACRBC may be due to the different curvatures of the inner and outer cylinder [6]. Here, we find that the time scale of the net azimuthal movement of the zonal flow is more than one order larger than that of the LSC, and more than two orders larger than the rotation time scale of the system ($1/\omega \simeq 10^{-1}$ s). Note that zonal flow is not observed at $Ra = 2.85\times10^{10}$, which may be due to the scale of plumes being smaller at larger Ra and the small plumes have been diffused at $R' \simeq 0.2$ (the position of the thermistor).

Next, assuming that the Taylor frozen hypothesis hold in the convective turbulence, Fig. 4b shows the temperature frequency power spectra (PS) $P(f)$ for the four Ra. The peak near the low-frequency end indicates the frequency $f_0 = \tau_0^{-1}$ of the zonal flow. Unexpectedly, a clear scaling of $P(f) \sim f^{-5}$ is observed for each Ra at $2 \lesssim f \lesssim 10$. This is more evident from the compensated spectra P/f^{-5} plotted in the inset of Fig. 4b. As mentioned in Sect. 1, the cascade mechanism of $E(k) \sim k^{-5}$ has been observed in some geophysical and astrophysical studies [25, 31-33], which results from turbulence in equilibrium with Rossby waves (zonal flow). One possible different point is that ACRBC has flat top and bottom plates, while the studies of geophysics and astrophysics have a so-called topographic-β effect due to the northward gradient of the Coriolis frequency $f_c = 2\omega\sin\theta$, where θ is the latitude. However, we note that because of the no-slip boundary conditions on the top and bottom plates and Ekman pumping effects [34], the topographic-β effect may also exist in ACRBC. The flow in ACRBC is similar to the flow in the equatorial region ($\theta = 0°$) of the planets. And we can estimate the Rhines frequency f_β at which the inverse cascade ceases. Combining Eqs. (1) and (11), (12),

$$l_\beta = 2\pi/k_\beta, \qquad f_\beta = U/L\,, \tag{11}$$

$$\beta = \mathrm{d}(f_c)/\mathrm{d}\theta = 2\omega\cos\theta, \qquad \theta = 0°\,, \tag{12}$$

we can obtain the Rhines frequency

$$f_\beta = \frac{1}{2\pi}\sqrt{U\omega}\,, \tag{13}$$

where U is the r.m.s. fluid velocity [26]. Here the velocity of the LSC (10) can be used as the characteristic velocity of the flow. The Rhines frequencies for each Ra are marked by vertical lines in Fig. 4. The magnitude of f_β is around half of a decade smaller than the smallest frequency of the –5 scaling range. Note that the Rhines scale in ACRBC is basically consistent with the previous study on zonal flow [25].

The small-scale dynamics in ACRBC may be a combination of buoyancy and rotation effects. The strong rotation leads to the very steep scaling of the PS so the turbulent eddies cannot cascade downward to small scales. The eddies may inverse cascade and evolve into zonal flows (Rossby waves). The merged large scales eddies may be dominated by centrifugal buoyancy at low frequency. At last, the energy is probably dissipated by Ekman friction with the solid walls. At a frequency larger than 10, the noise increases so the cutoff frequency is around 10. Thus further study for a much larger sampling rate is needed, which may give an even wider range of –5 scaling.

3.2 Velocity fluctuation

The measurement position of the LDV cannot corotate with the rotating reference frame as the thermistor. So the time series of the velocity $u(t)$ includes all the azimuthal positions. In order to decouple the azimuthal and time series of the velocity, we first set the initial position of the probe as ϕ_0. Secondly, the azimuthal region (2π) is equally divided into

1500 parts. Thirdly, the measured point at t has a phase of $\omega t + \phi_0$, and we transfer the phase to $[\phi_0, \phi_0 + 2\pi]$ according to $\omega t' + \phi_0 = (\omega t + \phi_0) - k \cdot (2\pi)$, where k is a non-negative integer. Fourthly, we take the mean of all data points in each part. The time series of u_r includes more than 3370000 velocity points for all cases, and the data points in each azimuthal interval are more than 2000 points. So the statistics for studying the azimuthal profile of u_r are enough.

Figure 5a shows the azimuthal distribution of the time-averaged radial velocity $\langle u_r \rangle_t$ at $z = 0.5H$ and three different radial positions. It is found that most u_r in the outer (inner) mixing zone have positive (negative) velocities, which suggests that more inward (outward) moving plumes exist in the outer (inner) mixing zone. Here we note that because the measured plane is not exactly parallel to the ϕr-plane, the mean of $\langle u_r \rangle_t$ at the three radial positions is slightly larger than zero. In addition, the previous study found that there are four pairs of convection rolls in this parameter range (see the experimental snapshot in Fig. 4A of Jiang et al. [4]). If each of the pairs of convection rolls is basically fixed at their azimuthal positions, the azimuthal distribution of $\langle u_r \rangle_t$ should have peaks and troughs in the mixing zone (dashed lines in Fig. 5a). Here, the dashed line uses the distribution function $u_r(\phi) = (u_r)_0 + A\cos(\phi\pi/2 + \phi_0)$ found in classical RBC [35, 36], which includes no zonal flow effect. In addition, the sinusoidal-like profile of $\langle u_r \rangle_t$ is verified by the DNS data without zonal flow from our previous study [7]. The amplitude A adopts the mean of the typical large positive and negative values of the time series of u_r. While at $Ra = 4.05 \times 10^9$, $\langle u_r \rangle_t$ basically have no peaks and troughs, suggesting that zonal flow pushes the azimuthal movement of the convection rolls and the azimuthal positions of plumes are not fixed (see Fig. 5b). The physical mechanism of zonal flow may result from the radius ratio effect and the Coriolis force (discussed in Ref. [6]). The azimuthal distributions of $\langle u_r \rangle_t$ for other cases are similar, which suggests zonal flow exists in the present parameter range. The further evidence of the existence of zonal flow by the velocity measurement is consistent with the mechanism of the "–5" scaling of the temperature spectra discussed in Sect. 3.1.

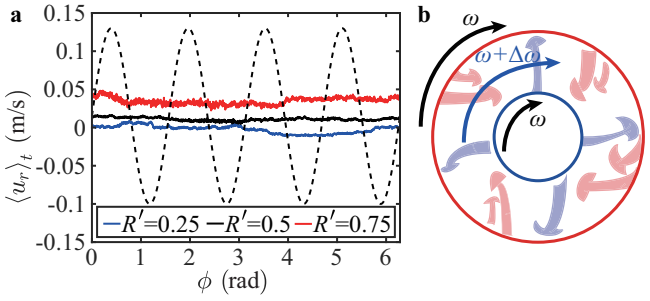

Figure 5 **a** Azimuthal distribution of $\langle u_r \rangle_t$ at different radial positions for $Ra = 4.05 \times 10^9$, $Ek = 6.88 \times 10^{-7}$. The dashed line is the possible azimuthal distribution of u_r if no zonal flow exists. **b** Sketch of the flow structures in ACRBC. The black arrows show that the two cylinders rotate with the same angular velocity ω. The blue arrow indicates the convection rolls revolve in the prograde direction around the axis with a faster rotation rate $\omega + \Delta\omega$ than the background rotation of the experimental system, which is the so-called zonal flow.

Next, let us discuss the PDF statistics of radial velocity fluctuation. Similar to the temperature fluctuation, the normalized radial velocity fluctuation is defined as $\delta u_r/\sigma_{u_r} = [u_r(t) - \langle u_r \rangle_t]/\left\langle (u_r(t) - \langle u_r \rangle_t)^2 \right\rangle^{1/2}$. As shown in Fig. 6, the shapes of PDF for different Ra are similar. The PDFs of δu_r are more sensitive to the radial position. Figure 6a shows that at $R' \simeq 0.75$, the PDF of $\delta u_r/\sigma_{u_r}$ has a core distribution similar to standard Gaussian function (7) and the tails positioned between the standard Gaussian function (7) and an exponential function (6) suggested by He et al. [12]. The positive tail is more approximate to the exponential function, suggesting that more warm plumes move from the outer cylinder to the inner cylinder in the outer mixing zone. Here, the theoretical model (8) is also used for fitting the PDF of velocity fluctuations. The fitted parameters are listed in Table II (documented in Appendix B). The fitted result $\alpha_c > \alpha_w$ reveals that the fluctuations contributed by the warm plumes are larger than the cold plumes. In addition, $\beta < 0.1$ indicates that the intermittency effect in ACRBC is also very weak for velocity fluctuations. Figure 6b and c shows that at $R' \simeq 0.5$ and 0.25, the PDFs of $\delta u_r/\sigma_{u_r}$ are both similar to the exponential distribution. The long exponential tail has the amplitude varied by more than 5 decades, which falls off much slower than a Gaussian. The exponential PDF indicates that more large fluctuations occur, which is probably produced by the thermal plumes. The exponential PDF has been observed in traditional RBC [12,13,20,21], so the PDF statistics of the fluctuations of radial velocity reveal that the dynamics of ACRBC are similar to traditional RBC.

Since the PDF in the outer mixing zone is different from that of the other two positions, we concentrate on the outer mixing zone ($R'_L/L \equiv (r_L - R_o)/L \in [0.025, 0.2]$) and measure the radial profile of the r.m.s. of the radial and azimuthal velocity fluctuations (Fig. 7). As discussed before, in this range of Ra, the thickness of thermal BL $\delta_{\text{th}}/L \simeq 0.005$. A small angle between the two beams of LDV leads to the largest radial position of the probe being at $R'_L/L \simeq 0.025$, so the profiles cannot include the BL. Figure 7a shows σ_{u_r} is basically independent on R'_L/L at $R'_L/L \lesssim 0.06$, and then σ_{u_r} decreases with the increase of R'_L/L at $0.06 \lesssim R'_L/L \lesssim 0.125$. When $R'_L/L \gtrsim 0.125$, σ_{u_r} transitions to increase with increasing R'_L/L. For σ_{u_ϕ} (Fig. 7b), the transition position is at $R'_L/L \simeq 0.15$, which is similar to that of σ_{u_r}. The magnitude of σ_{u_ϕ} first decreases with the increase of R'_L/L at $R'_L/L \lesssim 0.15$, and then increases with increasing R'_L/L at

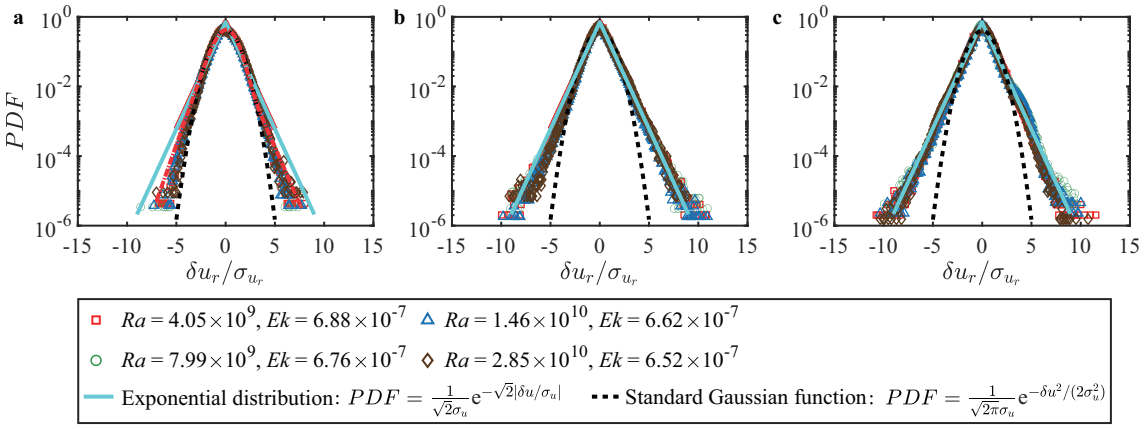

Figure 6 The PDF of $\delta u_r/\sigma_{u_r}$ for different values of Ra. The measurements are conducted in three different regions with **a** $R' \simeq 0.75$ (outer mixing zone), **b** $R' \simeq 0.5$ (cell centre), and **c** $R' \simeq 0.25$ (inner mixing zone). The black dashed lines in **a**-**c** show the Gaussian function given in Eq. (7). The celeste solid lines in **a**-**c** are the exponential function given in Eq. (6). The red dash-dotted line in **a** is the best fit of Eq. (8) to the PDF data points. The fitted values of the parameters are listed in Table II (documented in Appendix B).

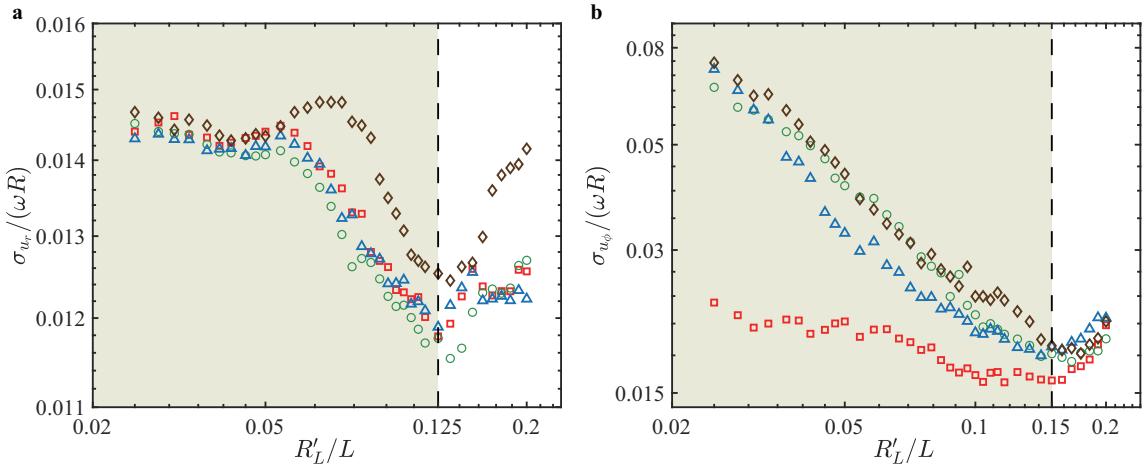

Figure 7 Normalized r.m.s. of the velocity fluctuation as a function of the normalized radial position $R'_L/L \equiv (r_L - R_o)/L \in [0.025, 0.2]$ for different Ra. **a** Radial velocity; **b** azimuthal velocity. The shaded and white areas correspond to the near-plate and near-bulk mixing zone, respectively. The colors and shapes of the symbols share the same conditions as Fig. 6.

$R'_L/L \gtrsim 0.15$. In the present parameter range, the variations of velocity fluctuation on R'_L/L for different Ra are similar. Note that at $Ra = 4.05 \times 10^9$, the slope of the profile of σ_{u_ϕ} is smaller than the other cases, which may be due to the low data rate of the azimuthal velocity for the case with a small temperature difference.

According to the transition point, the mixing zone is divided into two sub-regions which are the near-plate mixing zone ($\delta_{\text{th}} \lesssim R'_L/L \lesssim 0.125$) and near-bulk mixing zone ($0.125 \lesssim R'_L/L \lesssim 0.3$). In the near-plate mixing zone, there may only exist warm thermal plumes, which means cold plumes cannot travel to this region. The decrease of σ_{u_r} with increasing R'_L/L (Fig. 7a) indicates that the strength of warm plumes gradually becomes weaker with increasing R'_L/L because of the thermal diffusion. Furthermore, the azimuthal movement of the LSC in the near-plate mixing zone gradually becomes weaker for larger R'_L/L (Fig. 7b), which suggests the azimuthal velocity properties of the convection roll in ACRBC is like "fly-wheel-like" structure. In the near-bulk mixing zone, the reason for the increase of σ_{u_r} with increasing R'_L/L (Fig. 7a) is probably the appearance of cold plumes in this region. The inward warm plumes and outward cold plumes lead to the r.m.s. of the σ_{u_r} becoming increased. In addition, σ_{u_ϕ} increases at $R'_L/L \gtrsim 0.15$ (Fig. 7b), which is different from traditional RBC since the azimuthal movement of plumes in the bulk region is very weak in traditional RBC. However, Coriolis force in ACRBC could deflect the plumes moving in the radial direction. So the increase of σ_{u_ϕ} may result from the deflection of the radial movement of plumes. We note that similar profiles of the r.m.s. of the radial velocity were also found in traditional RBC measured by particle image velocimetry [37]. And the "fly-wheel-like" structure of the azimuthal velocity was observed in turbulent RBC in a thin vertical disk [38, 39].

4. Conclusion

We present an analysis of the temperature and velocity fluctuation in ACRBC, by means of small thermistors and LDV, with Ra varying from 4.05×10^9 to 2.85×10^{10}, fixed $Ek \simeq 6.7 \times 10^{-7}$, $Pr \simeq 4.2$, and radius ratio $\eta = 0.5$. Major findings are summarized as follows:

Firstly, the shapes of the PDFs of $\delta T/\sigma_T$ at a position in the inner mixing zone for $Ra \lesssim 1.46 \times 10^{10}$ are similar, which have large negative wings. These large negative excursions may result from the cold plumes. At $Ra = 2.85 \times 10^{10}$, the PDF changes to a Gaussian-like cap with exponential tails. The different PDF for high Ra may be due to the scale of plumes becoming small.

Secondly, the autocorrelation function of $\delta T(t)$ shows obvious periodic-like properties at $Ra \lesssim 1.46 \times 10^{10}$. We consider that is due to the zonal flow, which pushes the azimuthal movement of the cold plumes. The time scale of zonal flow is much larger than the large-scale circulation and the rotating system. In addition, assuming the Taylor frozen hypothesis, the temperature power spectra show a clear scaling of $P(f) \sim f^{-5}$ for different Ra. So the cascade mechanism of the convective turbulence is affected by the balance of turbulence and zonal flow. The Rhines scale f_β is about half of a decade larger than the largest scale of the –5 scaling range, which is basically consistent with the previous experimental results in the study of zonal flow in the astrophysical community.

Thirdly, it is found that the azimuthal distributions of the time-averaged radial velocity $\langle u_r \rangle_t(r_0,\phi,z_0)$ at different radial positions do not have obvious peaks and troughs, which also confirms the dynamics of zonal flow in ACRBC in the present parameter range. The PDFs of $\delta u_r/\sigma_{u_r}$ are basically independent on Ra. The shapes of PDFs at the midpoint and inner mixing zone are both consistent with the exponential distribution. While the tails of the PDFs in the outer mixing zone are positioned between the Gaussian function and exponential function. The exponential tails indicate that the fluctuations in ACRBC are similar to that of traditional RBC from the perspective of statistics. In addition, the profiles of the r.m.s. of the radial velocity and azimuthal velocity in the outer mixing zone are also found to be similar to traditional RBC, except that σ_{u_ϕ} increases with increasing R'_L/L in the near-bulk mixing zone, which is different from traditional RBC. The difference may be due to the Coriolis force in ACRBC deflecting the radial movement of plumes.

The statistics of the turbulent flow of ACRBC are similar to traditional RBC. And note that the additional rotation effects and boundary conditions of ACRBC are more similar to the convective turbulence on the planets (equatorial region). In addition, the effects of supergravity on thermal turbulence increase the buoyancy significantly. The physical mechanism behind the rapidly rotating convective turbulence is very rich, which may be affected by the buoyancy and Coriolis force. Hence, more studies and explorations are needed to further understand the flow properties in ACRBC.

Author contributions *Chao Sun and Quan Zhou designed the research. Dongpu Wang and Jing Liu wrote the first draft of the manuscript. Dongpu Wang set up the experiment set-up and processed the experiment data. Chao Sun and Quan Zhou helped organize the manuscript. All authors revised and edited the final version.*

Acknowledgements *This work was supported by the National Natural Science Foundation of China (Grant Nos. 11988102 and 91852202), and Tencent Foundation through the XPLORER PRIZE.*

1 G. Ahlers, S. Grossmann, and D. Lohse, Heat transfer and large scale dynamics in turbulent Rayleigh-Bénard convection, Rev. Mod. Phys. **81**, 503 (2009), arXiv: 0811.0471.
2 X. Zhu, and Q. Zhou, Flow structures of turbulent Rayleigh-Bénard convection in annular cells with aspect ratio one and larger, Acta Mech. Sin. **37**, 1291 (2021).
3 J. Z. Wu, B. F. Wang, and Q. Zhou, Massive heat transfer enhancement of Rayleigh-Bénard turbulence over rough surfaces and under horizontal vibration, Acta Mech. Sin. **38**, 321319 (2022).
4 H. Jiang, X. Zhu, D. Wang, S. G. Huisman, and C. Sun, Supergravitational turbulent thermal convection, Sci. Adv. **6**, eabb8676 (2020), arXiv: 2010.07189.
5 A. Rouhi, D. Lohse, I. Marusic, C. Sun, and D. Chung, Coriolis effect on centrifugal buoyancy-driven convection in a thin cylindrical shell, J. Fluid Mech. **910**, A32 (2021).
6 D. Wang, H. Jiang, S. Liu, X. Zhu, and C. Sun, Effects of radius ratio on annular centrifugal Rayleigh-Bénard convection, J. Fluid Mech. **930**, A19 (2022).
7 D. Wang, S. Liu, Q. Zhou, and C. Sun, Spectra and structure functions of the temperature and velocity fields in supergravitational thermal turbulence, Phys. Fluids **34**, 055108 (2022).
8 D. Lohse, and K. Q. Xia, Small-scale properties of turbulent Rayleigh-Bénard convection, Annu. Rev. Fluid Mech. **42**, 335 (2010).
9 M. K. Verma, A. Kumar, and A. Pandey, Phenomenology of buoyancy-driven turbulence: Recent results, New J. Phys. **19**, 025012 (2017), arXiv: 1611.09489.
10 Y. Wang, X. He, and P. Tong, Turbulent temperature fluctuations in a closed Rayleigh-Bénard convection cell, J. Fluid Mech. **874**, 263 (2019).
11 Y. Wang, Y. Wei, P. Tong, and X. He, Collective effect of thermal plumes on temperature fluctuations in a closed Rayleigh-Bénard convection cell, J. Fluid Mech. **934**, A13 (2022).
12 X. He, Y. Wang, and P. Tong, Dynamic heterogeneity and conditional statistics of non-Gaussian temperature fluctuations in turbulent thermal convection, Phys. Rev. Fluids **3**, 052401 (2018).
13 P. Wei, and G. Ahlers, On the nature of fluctuations in turbulent Rayleigh-Bénard convection at large Prandtl numbers, J. Fluid Mech. **802**, 203 (2016).
14 Y. C. Xie, B. Y. C. Cheng, Y. B. Hu, and K. Q. Xia, Universal fluctuations in the bulk of Rayleigh-Bénard turbulence, J. Fluid Mech. **878**, R1 (2019).
15 S. Q. Zhou, and K. Q. Xia, Scaling properties of the temperature field in convective turbulence, Phys. Rev. Lett. **87**, 064501 (2001).
16 T. Mashiko, Y. Tsuji, T. Mizuno, and M. Sano, Instantaneous measurement of velocity fields in developed thermal turbulence in mercury, Phys. Rev. E **69**, 036306 (2004), arXiv: cond-mat/0310445.
17 S. B. Pope, Chapter 3—The Statistical Description of Turbulent Flows, Turbulent Flows (Cambridge University Press, Cambridge, 2000), pp.

34-82.
18 L. P. Kadanoff, Turbulent heat flow: Structures and scaling, Phys. Today **54**, 34 (2001).
19 A. Belmonte, A. Tilgner, and A. Libchaber, Temperature and velocity boundary layers in turbulent convection, Phys. Rev. E **50**, 269 (1994).
20 J. J. Niemela, L. Skrbek, K. R. Sreenivasan, and R. J. Donnelly, Turbulent convection at very high Rayleigh numbers, Nature **404**, 837 (2000).
21 X. He, P. Tong, and K. Q. Xia, Measured Thermal Dissipation Field in Turbulent Rayleigh-Bénard Convection, Phys. Rev. Lett. **98**, 144501 (2007).
22 S. Q. Zhou, and K. Q. Xia, Plume statistics in thermal turbulence: Mixing of an active scalar, Phys. Rev. Lett. **89**, 184502 (2002).
23 H. P. Greenspan, The Theory of Rotating Flows (Cambridge University Press, Cambridge, 1968).
24 M. Heimpel, J. Aurnou, and J. Wicht, Simulation of equatorial and high-latitude jets on Jupiter in a deep convection model, Nature **438**, 193 (2005).
25 P. L. Read, Y. H. Yamazaki, S. R. Lewis, P. D. Williams, K. Miki-Yamazaki, J. Sommeria, H. Didelle, and A. Fincham, Jupiter's and Saturn's convectively driven banded jets in the laboratory, Geophys. Res. Lett. **31**, L22701 (2004).
26 P. B. Rhines, Waves and turbulence on a beta-plane, J. Fluid Mech. **69**, 417 (1975).
27 J. M. Aurnou, M. A. Calkins, J. S. Cheng, K. Julien, E. M. King, D. Nieves, K. M. Soderlund, and S. Stellmach, Rotating convective turbulence in Earth and planetary cores, Phys. Earth Planet. Inter. **246**, 52 (2015).
28 G. Schubert, Treatise on Geophysics (Elsevier, 2015).
29 H. Jiang, X. Zhu, V. Mathai, R. Verzicco, D. Lohse, and C. Sun, Controlling heat transport and flow structures in thermal turbulence using ratchet surfaces, Phys. Rev. Lett. **120**, 044501 (2018), arXiv: 1712.09303.
30 Z. Wang, V. Mathai, and C. Sun, Self-sustained biphasic catalytic particle turbulence, Nat. Commun. **10**, 3333 (2019).
31 S. Sukoriansky, B. Galperin, and N. Dikovskaya, Universal spectrum of two-dimensional turbulence on a rotating sphere and some basic features of atmospheric circulation on giant planets, Phys. Rev. Lett. **89**, 124501 (2002).
32 C. Guervilly, P. Cardin, and N. Schaeffer, Turbulent convective length scale in planetary cores, Nature **570**, 368 (2019), arXiv: 1810.09553.
33 N. Schaeffer, and P. Cardin, Rossby-wave turbulence in a rapidly rotating sphere, Nonlin. Processes Geophys. **12**, 947 (2005).
34 B. Cushman-Roisin, and J.-M. Beckers, Introduction to Geophysical Fluid Dynamics (Academic Press, New York, 2009).
35 E. Brown, A. Nikolaenko, and G. Ahlers, Reorientation of the large-scale circulation in turbulent Rayleigh-Bénard Convection, Phys. Rev. Lett. **95**, 084503 (2005), arXiv: physics/0503162.
36 H. D. Xi, and K. Q. Xia, Cessations and reversals of the large-scale circulation in turbulent thermal convection, Phys. Rev. E **75**, 066307 (2007).
37 C. Sun, Y. H. Cheung, and K. Q. Xia, Experimental studies of the viscous boundary layer properties in turbulent Rayleigh-Bénard convection, J. Fluid Mech. **605**, 79 (2008).
38 H. Song, E. Villermaux, and P. Tong, Coherent Oscillations of Turbulent Rayleigh-Bénard Convection in a Thin Vertical Disk, Phys. Rev. Lett. **106**, 184504 (2011).
39 Y. Wang, P. Y. Lai, H. Song, and P. Tong, Mechanism of large-scale flow reversals in turbulent thermal convection, Sci. Adv. **4**, eaat7480 (2018).

超重力湍流对流中的温度和速度脉动统计特性研究

王东璞, 刘婧, 周全, 孙超

摘要 本文通过实验研究了超重力湍流对流系统中的温度脉动和速度脉动. 负尖峰信号在温度脉动时间序列中周期性地出现, 这可能是由旋转坐标系下的所谓的纬向流推动冷羽流的周向运动造成的. 周期τ_0随着瑞利数(Ra)的增加而略微减小, 并且τ_0比大尺度环流的时间尺度大超过一个数量级. 此外, 对于不同Ra数, 温度脉动能谱在$2 \lesssim f \lesssim 10$范围内遵循$P(f) \sim f^{-5}$, 这意味着超重力湍流对流中可能存在湍流与纬向流相平衡的反向能量级串, 本研究还计算了反向级串的截止频率莱茵(Rhines)频率f_β, f_β比–5 次方斜率能谱范围的最低频率还低半个数量级左右. 本研究还发现时间平均径向速度的周向分布没有明显的峰谷, 这为纬向流的存在性提供了进一步的证据. 此外, 我们发现该系统中的温度和速度脉动的概率密度分布可以通过Wang等人提出的经典瑞利-伯纳德(Rayleigh-Bénard)对流的理论模型(Wang等, 2019, 2022)较好地拟合和分析.